# On the Dynamical Mechanisms Governing El Niño–Southern Oscillation Irregularity

JUDITH BERNER

*National Center for Atmospheric Research, Boulder, Colorado*

PRASHANT D. SARDESHMUKH

*Cooperative Institute for Research in Environmental Sciences, Boulder, Colorado*

HANNAH M. CHRISTENSEN

*National Center for Atmospheric Research, Boulder, Colorado*

(Manuscript received 22 April 2018, in final form 14 July 2018)

## ABSTRACT

This study investigates the mechanisms by which short time-scale perturbations to atmospheric processes can affect El Niño–Southern Oscillation (ENSO) in climate models. To this end a control simulation of NCAR's Community Climate System Model is compared to a simulation in which the model's atmospheric diabatic tendencies are perturbed every time step using a Stochastically Perturbed Parameterized Tendencies (SPPT) scheme. The SPPT simulation compares better with ECMWF's twentieth-century reanalysis in having lower interannual sea surface temperature (SST) variability and more irregular transitions between El Niño and La Niña states, as expressed by a broader, less peaked spectrum. Reduced-order linear inverse models (LIMs) derived from the 1-month lag covariances of selected tropical variables yield good representations of tropical interannual variability in the two simulations. In particular, the basic features of ENSO are captured by the LIM's least damped oscillatory eigenmode. SPPT reduces the damping time scale of this eigenmode from 17 to 11 months, which is in better agreement with the 8 months obtained from reanalyses. This noise-induced stabilization is consistent with perturbations to the frequency of the ENSO eigenmode and explains the broadening of the SST spectrum (i.e., the greater ENSO irregularity). Although the improvement in ENSO shown here was achieved through stochastic physics parameterizations, it is possible that similar improvements could be realized through changes in deterministic parameterizations or higher numerical resolution. It is suggested that LIMs could provide useful insight into model sensitivities, uncertainties, and biases also in those cases.

## 1. Introduction

El Niño–Southern Oscillation (ENSO) is the dominant mode of tropical variability on interannual time scales. It consists of an irregular oscillation of sea surface temperature anomalies over the tropical eastern Pacific Ocean, with a periodicity in the 3–7-yr range. Through atmospheric teleconnections, ENSO impacts weather across the globe and is the leading source of skill for seasonal and interannual forecasts. It is imperative that general climate models (GCMs) capture this source of predictability.

Despite the importance of ENSO, state-of-the-art coupled climate models show a wide range of ENSO behavior (Guilyardi et al. 2009; Flato et al. 2013), with differences not only from model to model, but even from one model version to the next. In general, the models in phase 5 of the Coupled Model Intercomparison Project (CMIP5) show large deficiencies in ENSO amplitudes, spatial structures, and temporal variability (Flato et al. 2013).

Many authors have demonstrated the importance of small-scale atmospheric variability in ENSO dynamics (Penland and Sardeshmukh 1995; Flügel et al. 2004; Yeh

---

Supplemental information related to this paper is available at the Journals Online website: https://doi.org/10.1175/JCLI-D-18-0243.s1.

---

*Corresponding author*: Judith Berner, berner@ucar.edu

DOI: 10.1175/JCLI-D-18-0243.1

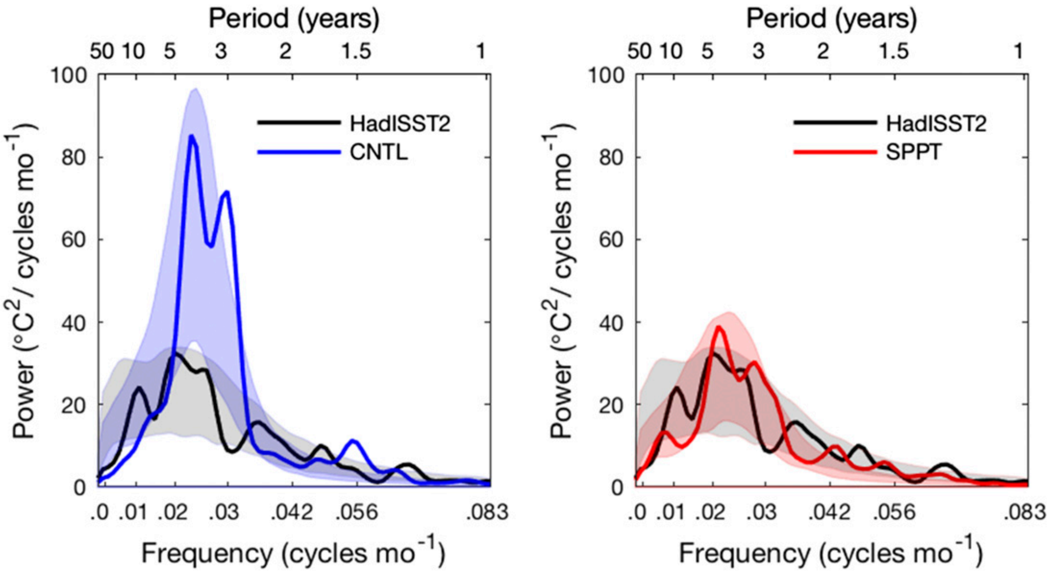

FIG. 1. Power spectrum of the Niño-3.4 index, defined as the monthly SST anomaly averaged over 5°S–5°N and 170°E–120°W, for HadISST2 observations (black), CNTL (blue), and SPPT (red). The top axis indicates period in years, and the bottom axis indicates frequency in cycles per month. The shading denotes the spectral range obtained by sampling realizations from LIMs fitted to CNTL, SPPT, and HadISST (see text). After Christensen et al. (2017).

and Kirtman 2006). The low resolution of current coupled climate models (of order 1°–2°) is inadequate for capturing this small-scale variability. Increasing the resolution has been shown to improve the representation of ENSO (e.g., Small et al. 2014) but this remains often too computationally expensive for multidecadal climate projections.

An alternative to represent unresolved subgridscale variability is through the use of stochastic parameterization schemes (Palmer 2001). Models with such schemes represent subgridscale atmospheric processes as a predictable deterministic plus an unpredictable stochastic component. Stochastic parameterizations have been widely used in the weather and seasonal forecasting community because of their beneficial impact on probabilistic forecast reliability (e.g., Berner et al. 2009; Leutbecher et al. 2017; Weisheimer et al. 2014). Despite their beneficial impact on weather and seasonal predictions, the use of stochastic parameterizations in climate models remains a scientific frontier (Berner et al. 2017), since model error on longer time scales tends to be dominated by deterministic rather than random model error.

Of particular relevance to this study are the findings by Christensen et al. (2017), who demonstrated that stochastic perturbations to the atmospheric component of the Community Climate System Model, version 4 (CCSM4), leads to remarkably improved ENSO variability in the model. Without stochastic perturbations, the model ENSO is too regular and too strong. Including the stochastic perturbations improves the power spectrum of SSTs in the Niño-3.4 region [Fig. 1, after Christensen et al. (2017)] and the variance of monthly SST and wind anomalies is also in better agreement with observations [Fig. 2, cf. Figs. 5 and 6 of Christensen et al. (2017)]. Note that Fig. 2 shows the variance difference of a control simulation (CNTL) from ECMWF Re-Analysis of the 20th-Century Climate (ERA20C) indicating that the variance in the control simulation is too strong. The stochastically perturbed parameterization tendency (SPPT) reduces the variance leading to a better agreement with the reanalysis.

Christensen et al. (2017) proposed a number of possible mechanisms for this improvement, but a complete understanding was outside the scope of that study. In the present study, we will reexamine these coupled simulations. Our aim is to understand how fast fluctuations on weather time scales (as mimicked by the stochastic parameterization) can impact interannual tropical variability. In particular, we will address the mechanisms by which perturbations to the atmosphere can

- reduce SST and wind variability, and
- broaden the spectrum of tropical SSTs, that is, increase ENSO irregularity.

Note that according to the Wiener–Khinchin theorem (e.g., Gardiner 1983), the power spectrum is the Fourier transform of the autocovariance function, so that a

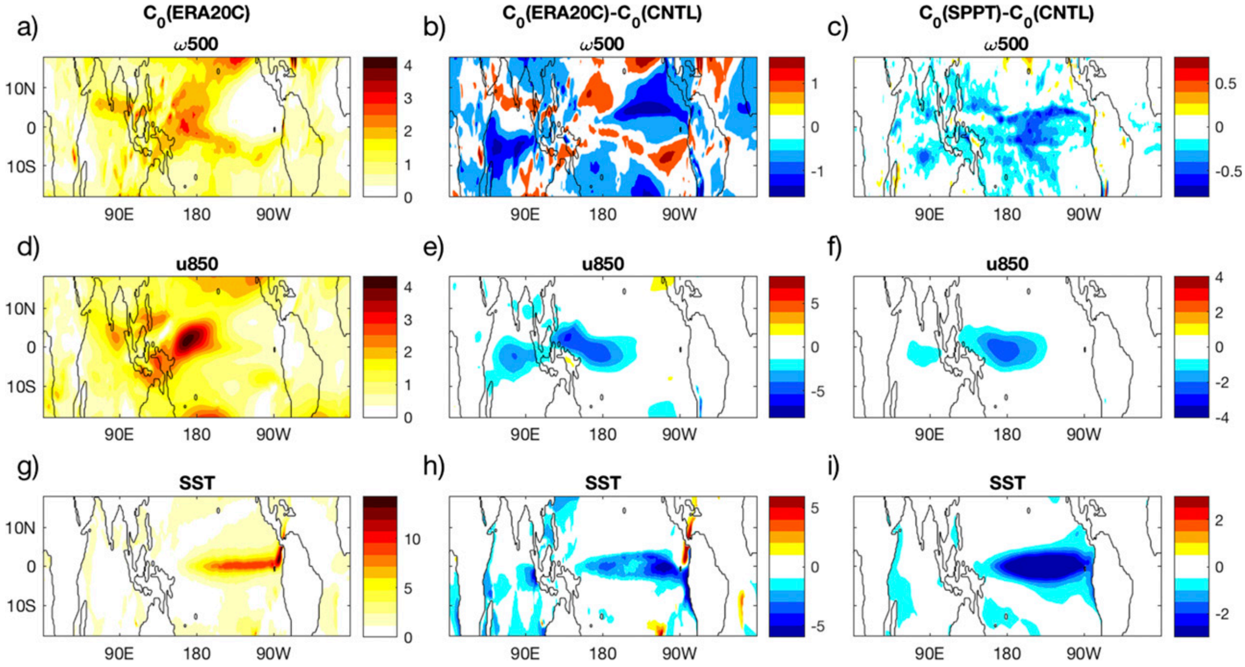

FIG. 2. Variance of monthly anomalies over the period 1900–2010 for (a) $\omega$500, (d) u850, and (g) SST in ERA20C. (b),(e),(h) Difference in variance between ERA20C and CNTL, where CNTL spans the years 1870–2004. (c),(f),(i) Difference in variance between SPPT and CNTL for the period 1870–2004. Note that the contour interval in (c), (f), and (i) is half that of (b), (e), and (h).

change in temporal autocovariance translates directly to a change in the spectrum.

To gain insights into the dynamical mechanisms leading to the change in ENSO variability, we fit linear inverse models (LIM) to the two climate simulations and subsequently compare the LIMs governing ENSO dynamics and its weather forcing. Linear inverse models (Xu and von Storch 1990; Penland and Magorian 1993; Latif et al. 1994; Wu et al. 1994; Balmaseda et al. 1995) have been demonstrated to show excellent skill in predicting tropical SST variability (Penland and Sardeshmukh 1995; Newman et al. 2009, 2011; Alexander et al. 2008; Newman and Sardeshmukh 2017) and have also been applied to observed Atlantic sea surface temperatures (Zanna 2012). In particular, the least damped oscillatory eigenmode, or principal oscillation pattern (POP; von Storch et al. 1988, 1995; Penland 1989) captures the basic features of ENSO (Penland and Magorian 1993; Penland and Sardeshmukh 1995; Gehne et al. 2014).

Kleeman (2011) performs a comprehensive spectral analysis for a generalized class of stochastic models including LIM and applies it to the two-dimensional stochastically forced oscillator, which can be interpreted as ENSO POP. Different from previous studies, which mainly focus on using LIMs as predictive models, we exploit their utility here also as a general tool to investigate model differences and model sensitivities (Shin et al. 2010).

Given the underlying assumptions, LIMs are fundamentally limited to which degree they can model non-Gaussian and nonlinear features. For example, LIMs cannot capture the apparent greater persistence of La Niña versus El Niño events (DiNezio and Deser 2014). In their simplest form, the noise is assumed to be state independent, the resulting distributions Gaussian, and thus unable to capture the skewness in, for example, the distribution of the Niño-3.4 index (Burgers and Stephenson 1999). However, the inclusion of state-dependent noise terms enables LIMs in principle to model skewed distributions (Sardeshmukh and Sura 2009).

The paper is organized as follows: the linear inverse modeling approach is summarized in section 2. A simple damped linear oscillator forced by white noise is used to illustrate the impact of perturbing the damping rate and frequency of the eigenmodes of a linear system. Datasets and the setup for the numerical experiments are introduced in section 3. Section 4 contains the results of fitting LIMs to the coupled climate simulations, followed by a discussion (section 5) and the conclusions (section 6).

## 2. Methodology and simple example

### a. *Damped linear system forced by additive white noise*

Before turning our attention to the evaluation of the coupled climate simulations, we introduce the linear inverse modeling framework and apply it to the simple example of the perturbed and unperturbed damped oscillator. Consider the following stochastically forced damped linear system:

$$\dot{\mathbf{x}} = \mathbf{L}\mathbf{x} + \mathbf{S}\boldsymbol{\varepsilon}, \tag{1}$$

where $\mathbf{x}(t)$ is the temporally evolving state variable and $\mathbf{L}$ is the deterministic linear feedback matrix. The external forcing consists of the additive white-noise forcing $\boldsymbol{\varepsilon}$ with noise amplitudes given by the matrix $\mathbf{S}$ with components $\sigma_{\varepsilon,ij}$. A linear inverse model of a nonlinear system is of the form in (1), in which the nonlinear tendency terms are approximated as linear terms plus noise.

The time evolution of such a system is given by the time-lag covariance matrix $C_{ij}(\tau) = \langle x_i(t+\tau)x_j(t)\rangle$ (Penland 1989):

$$\mathbf{C}(\tau) = e^{\mathbf{L}\tau}\mathbf{C}(0). \tag{2}$$

In the statistically stationary state, the covariance of the system, $\mathbf{C}_0 = \mathbf{C}(0)$, is completely determined by the linear operator $\mathbf{L}$ and the noise covariance matrix $\mathbf{Q} = \mathbf{S}\mathbf{S}^{\mathrm{T}}$ (Gardiner 1983; Farrell and Ioannou 1993; Penland and Matrosova 1994):

$$\mathbf{L}\mathbf{C}_0 + \mathbf{C}_0\mathbf{L}^{\mathrm{T}} + \mathbf{Q} = 0. \tag{3}$$

Equation (3) is called the Lyapunov equation and sometimes the fluctuation–dissipation relationship (FDR) and can be derived from the stationary solution of the Fokker–Planck equation for a system of the form in (1). Because $\mathbf{C}_0$ and $\mathbf{Q} = \mathbf{S}\mathbf{S}^{\mathrm{T}}$ are both positive-definite, (3) can be satisfied only if $\mathbf{L}$ is a stable operator (i.e., if its eigenvalues are either real and negative or come in complex conjugate pairs with negative real parts). Physically, (3) states that the equilibrium covariance of a system is given as a balance between the stable operator—acting to drive the system toward equilibrium—and the noise covariance matrix—forcing the system away from equilibrium (Penland and Matrosova 1994).

### b. *Damped linear system forced by additive and multiplicative white noise*

Now consider a system with the same linear feedback matrix, but with an additional state-dependent (multiplicative) noise forcing $\eta$ assumed to be linear in each component of the state $x_i$:

$$\dot{x}_i = L_{ij}x_j + \eta\sigma_{\eta,ij}x_j + \sigma_{\varepsilon,ij}\varepsilon_j. \tag{4}$$

Here, $\eta$ is a white-noise process with zero mean and unit standard deviation, and (4) can be written as

$$\dot{\mathbf{x}} = (\mathbf{L} + \mathbf{E}\eta)\,\mathbf{x} + \mathbf{S}\boldsymbol{\varepsilon}, \tag{5}$$

where the amplitudes of the multiplicative noise are given by the matrix $\mathbf{E}$ with components $\sigma_{\eta,ij}$.

The noise in (5) is a special case of the correlated additive and multiplicative (CAM) noise of Sardeshmukh and Sura (2009), namely, one that is multiplicative, but not correlated additive. Thus, the probability density of the process in (5) will be symmetric and not skewed as is the case for general CAM noise. For such a system, the covariance evolution and FDR in (2)–(3) are (see Sardeshmukh and Sura 2009)

$$\mathbf{C}(\tau) = e^{\mathbf{M}\tau}\mathbf{C}_0 \quad \text{and} \tag{6}$$

$$\mathbf{M}\mathbf{C}_0 + \mathbf{C}_0\mathbf{M}^{\mathrm{T}} + \tilde{\mathbf{Q}} = 0, \tag{7}$$

where the feedback matrix $\mathbf{M}$ and noise covariance matrix $\tilde{\mathbf{Q}}$ are given as

$$\mathbf{M} = \mathbf{L} + \frac{1}{2}\mathbf{E}^2 \quad \text{and} \tag{8}$$

$$\tilde{\mathbf{Q}} = \mathbf{S}\mathbf{S}^{\mathrm{T}} + \mathbf{E}\mathbf{C}_0\mathbf{E}^{\mathrm{T}}. \tag{9}$$

Note, that the effective feedback matrix $\mathbf{M}$ consists now of $\mathbf{L}$ plus a ''noise-induced drift'' $(1/2)\mathbf{E}^2$. Similarly, the noise covariance matrix has now two terms: $\mathbf{S}\mathbf{S}^{\mathrm{T}}$ from the additive noise forcing, and an additional term $\mathbf{E}\mathbf{C}_0\mathbf{E}^{\mathrm{T}}$ from the multiplicative noise forcing.

### c. *Example: The perturbed 2D-damped harmonic oscillator forced by additive white noise*

As a simple example we consider the damped harmonic oscillator, driven by additive white noise. Its evolution is given by (1) with

$$\mathbf{L} = \begin{pmatrix} -\nu & \omega \\ -\omega & -\nu \end{pmatrix}, \tag{10}$$

where $\nu > 0$ and $\omega$ denote the damping rate and frequency of the oscillation, respectively, and $T = 2\pi/\omega$ is the period. A sample time series of such a system is given in Fig. 3a. The eigenvalues of $\mathbf{L}$ form the complex conjugate pair:

$$\lambda_{1,2} = -\nu \pm i\omega.$$

In the absence of forcing, the solution of each component of the damped harmonic oscillator is given as

$$x(t) = e^{-\nu\tau}(\cos\omega\tau + i\sin\omega\tau).$$

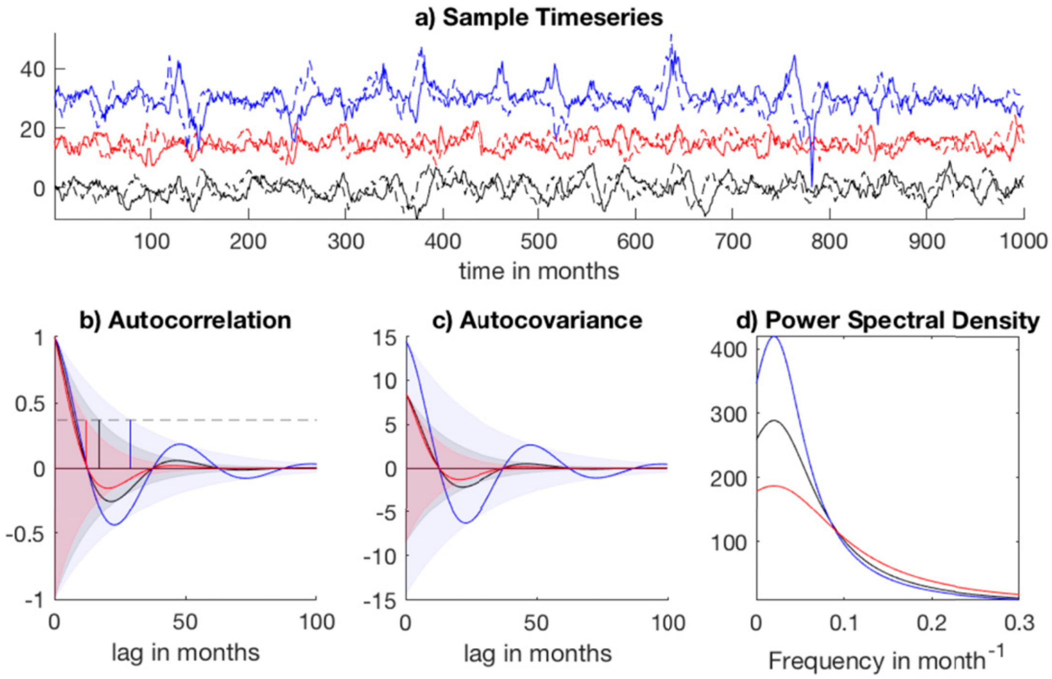

FIG. 3. (a) Sample time series of damped linear oscillators driven by additive and perturbed by multiplicative white noises. Oscillator with parameters damping rate $\nu = 1/17$ months and frequency $\omega = 1/50$ months driven by additive noise (black). Oscillator with additional multiplicative perturbations to the frequency (red). Oscillator with additional multiplicative perturbations to the damping rate (blue). The time series for the two components of the oscillator are indicated by solid and dashed lines, respectively. For easier reading, the blue and red curves are shifted upward by 15 and 30 units, respectively. (b) Autocorrelation and (c) autocovariance of the additively perturbed and additively and multiplicative perturbed oscillators. The shading in (b) and (c) denotes the autocorrelation and autocovariance of the amplitude of the oscillation, respectively. The decorrelation time $\tau_{d}$ by which the autocorrelation of the amplitude has decayed to $1/e$ (dashed line) is denoted as vertical line for each experiment. (d) Power spectra of the three cases.

The decorrelation time or damping time $\tau_{d}$ is defined as

$$\tau_{d,\mathrm{ref}} = \frac{1}{\nu}.$$

The stronger the damping rate $\nu$, the smaller the damping time $\tau_{d}$ and vice versa.[1] We note that the decorrelation time is equal to the negative inverse of the real part of the eigenvalue, so that knowing the eigenvalues $\lambda_{1,2}$ of the feedback matrix allows us to infer the temporal memory of the oscillator. If $\omega = 0$, there is no oscillation and the system governed by (10) describes two independent linearly damped processes forced by white noise, also called red-noise process.

If the noise is uncorrelated and has the same amplitude for each component, $\mathbf{Q} = [\sigma_\varepsilon^2, 0 \,|\, 0, \sigma_\varepsilon^2]$, we can solve (3) for the stationary covariance matrix:

$$\mathbf{C}_{0,\mathrm{ref}} = \begin{pmatrix} \dfrac{\sigma_\varepsilon^2}{2\nu} & 0 \\ 0 & \dfrac{\sigma_\varepsilon^2}{2\nu} \end{pmatrix}.$$

Next, consider the impact of perturbations to the linear operator. In particular, consider cases in which either the damping rate $\nu$ or frequency $\omega$ are perturbed by making the $\mathbf{E}$ matrix in (5) nonzero. The evolution of the perturbed system is then given by (5) with

$$\mathbf{E}_d = \begin{pmatrix} \sigma_\eta & 0 \\ 0 & \sigma_\eta \end{pmatrix} \quad \text{and} \quad \mathbf{E}_f = \begin{pmatrix} 0 & \sigma_\eta \\ -\sigma_\eta & 0 \end{pmatrix},$$

where the subscripts "$d$" and "$f$" denote the perturbations to the damping rate and frequency, respectively. Since $\mathbf{E}$ in both cases acts on the state $\mathbf{x}$, the perturbations are state dependent or multiplicative. Examples for time series of the perturbed linear oscillators are included in Fig. 3a. If the oscillator in (10) were to describe the oscillation of a pendulum, perturbing the frequency would be analogous to changing the length of

---

[1] Note again that $\nu$ refers to the damping *rate* and $\tau_{d}$ refers to the damping (or decorrelation) *time*.

the string, while perturbing the damping rate can be interpreted as changing the viscosity of the environment.

From (8) we calculate the noise-induced drift and effective feedback matrices to be

$$\frac{1}{2}\mathbf{E}_d^2 = \frac{1}{2}\begin{pmatrix} \sigma_\eta^2 & 0 \\ 0 & \sigma_\eta^2 \end{pmatrix} \quad \text{and} \quad \frac{1}{2}\mathbf{E}_f^2 = \frac{1}{2}\begin{pmatrix} -\sigma_\eta^2 & 0 \\ 0 & -\sigma_\eta^2 \end{pmatrix},$$

and

$$\mathbf{M}_d = \begin{pmatrix} -\nu + \frac{1}{2}\sigma_\eta^2 & \omega \\ -\omega & -\nu + \frac{1}{2}\sigma_\eta^2 \end{pmatrix} \quad \text{and}$$

$$\mathbf{M}_f = \begin{pmatrix} -\nu - \frac{1}{2}\sigma_\eta^2 & \omega \\ -\omega & -\nu - \frac{1}{2}\sigma_\eta^2 \end{pmatrix}, \tag{11}$$

with eigenvalues:

$$\lambda_{1,2}^d = -\nu + \frac{1}{2}\sigma_\eta^2 \pm i\omega \quad \text{and} \quad \lambda_{1,2}^f = -\nu - \frac{1}{2}\sigma_\eta^2 \pm i\omega. \tag{12}$$

The decorrelation time for each component is computed as the negative inverse of the real part of the eigenvalues as

$$\tau_{\mathscr{d},d} = \frac{1}{\nu - \frac{1}{2}\sigma_\eta^2} \quad \text{and} \quad \tau_{\mathscr{d},f} = \frac{1}{\nu + \frac{1}{2}\sigma_\eta^2}. \tag{13}$$

It is clear that perturbing the damping rate leads to an increase of temporal memory (destabilization), $\tau_{\mathscr{d},d} > \tau_{\mathscr{d},\mathrm{ref}}$, while perturbing the frequency leads to a decrease in memory (stabilization), $\tau_{\mathscr{d},f} < \tau_{\mathscr{d},\mathrm{ref}}$ (Fig. 3b). This is a direct consequence of the noise-induced drift, which acts effectively to increase the damping (in the case of perturbing the frequency $\omega$) or reduce it (in the case of perturbing the damping rate $\nu$) of the oscillation.

Finally, we compute the equilibrium covariance matrices by inserting (11) into the fluctuation dissipation relation in (7) and solving for $\mathbf{C}_0$:

$$\mathbf{C}_{0,d} = \begin{pmatrix} \frac{\sigma_\varepsilon^2}{2\nu - \sigma_\eta^2} & 0 \\ 0 & \frac{\sigma_\varepsilon^2}{2\nu - \sigma_\eta^2} \end{pmatrix} \quad \text{and} \quad \mathbf{C}_{0,f} = \begin{pmatrix} \frac{\sigma_\varepsilon^2}{2\nu} & 0 \\ 0 & \frac{\sigma_\varepsilon^2}{2\nu} \end{pmatrix}. \tag{14}$$

While for perturbations to the frequency, the equilibrium covariance matrix is the same as for the unperturbed oscillation, $\mathbf{C}_{0,f} = \mathbf{C}_{0,\mathrm{ref}}$, the variance increases when the damping rate is perturbed: $\mathbf{C}_{0,d} > \mathbf{C}_{0,\mathrm{ref}}$ (Fig. 3b).

The derivation reveals that the multiplicative noise introduces two terms in the denominator: the noise-induced drift and an additional term to the noise covariance matrix. For perturbations to the frequency, these two terms are of equal magnitude but opposite sign, so that they cancel each other. For perturbations to the damping rate, they have the same sign, leading to the $-\sigma_\eta^2$ in the denominator of the expression for the covariance.

Physically, the increase in variance—or energy—in the case of perturbing the damping rate can be understood by visualizing a pendulum. At maximum amplitude, perturbations increasing the amplitude will increase the potential energy, while perturbations toward the state of rest will increase the kinetic energy, both leading to an increase in energy and thus variance.

While the stabilizing influence of noise has been discussed in the geophysical contexts (e.g., by Sardeshmukh et al. 2001, 2003), this is to our best knowledge the first explicit application to an oscillator.

### *d. Spectra*

The spectral matrix $\mathbf{S}(f)$ of a system given by (5) is given as (Gardiner 1983; Kleeman 2011):

$$\mathbf{S}(f) = \frac{1}{2\pi}(\mathbf{M} + if)^{-1}\tilde{\mathbf{Q}}(\mathbf{M}^{\mathrm{T}} - if)^{-1}, \tag{15}$$

where $f$ is the frequency. For the case of a linear damped oscillator driven by additive white noise, in (10) $\mathbf{M} = \mathbf{L}$. For this system the spectrum of each component is given as

$$P(f) = \frac{\sigma_\varepsilon^2}{\nu^2 + (\omega \pm f)^2}. \tag{16}$$

If the eigenvalues $\lambda_{1/2}$ of $\mathbf{M}$ are purely real, then the spectrum is red with a maximum at $f = 0$. If the eigenvalues of $\mathbf{M}$ are complex, the spectrum has a maximum at $f = \omega$ and its width is a function of the damping rate $\nu$. The larger the damping rate, the broader and less peaked is the spectrum.

For the multiplicatively perturbed oscillators, $\mathbf{M} = \mathbf{L} + (1/2)\mathbf{E}^2$, and the component power spectral density is obtained by inserting (11) into (15) to give

$$P_d(f) = \frac{\sigma_\varepsilon^2\left(1 + \frac{\sigma_\eta^2}{2\nu - \sigma_\eta^2}\right)}{\left(\nu + \frac{1}{2}\sigma_\eta^2\right)^2 + (\omega \pm f)^2} \quad \text{and}$$

$$P_f(f) = \frac{\sigma_\varepsilon^2\left(1 - \frac{\sigma_\eta^2}{2\nu}\right)}{\left(\nu - \frac{1}{2}\sigma_\eta^2\right)^2 + (\omega \pm f)^2}. \tag{17}$$

The spectra for the multiplicatively perturbed oscillators for our examples are shown in Fig. 3d. We see that perturbations to the frequency $\omega$ result in a broader spectrum, while perturbations to the damping rate lead to a more pronounced spectral peak.

## 3. Model description and experiments

The numerical simulations of the coupled ocean–atmosphere system analyzed in this work are conducted with the CCSM4 developed by the National Center for Atmospheric Research (NCAR) and cover the period 1870–2004 (135 years). The atmospheric component is the Community Atmosphere Model, version 4 (Gent et al. 2011). All simulations were conducted with the finite-volume dynamical core at a resolution of 0.9° × 1.25° with 26 vertical levels and the use of observed carbon dioxide concentrations in the atmosphere. The ocean is simulated by the Parallel Ocean Program, version 2 (Danabasoglu et al. 2012), with 1.0° horizontal resolution and 40 levels in the vertical. It is also actively coupled to the Community Ice Code, version 4 (Hunke and Lipscomb 2008), at 1.0° resolution and the Community Land Model, version 4 (Lawrence et al. 2011).

Two experiments were conducted: a CNTL and a simulation where a stochastic parameterization scheme was used to represent unresolved atmospheric variability. The scheme used here is the widely used SPPT scheme, which perturbs the physical tendencies of temperature, zonal and meridional winds, and humidity at each time step with a multiplicative random coefficient (Buizza et al. 1999; Palmer et al. 2009):

$$\frac{\partial X}{\partial t} = D + (1 + r)\sum_i P_i. \qquad (18)$$

Here, $\partial X/\partial t$ denotes the total tendency in variable $X$, $D$ is the tendency from the dynamical core, $P_i$ is the tendency from the $i$th physics scheme, and $r$ is the Gaussian distributed zero-mean random perturbation field with spatial and temporal correlations. Depending on the implementation, the SPPT scheme uses up to three patterns with different spatial and time scales. For simplicity, we use here only a single perturbation field with a spatial decorrelation length scale of 500 km and decorrelation time scale of 6 h, which corresponds to the fastest evolving perturbation pattern of Palmer et al. (2009). No effort was made to optimize the spatial and temporal correlations of the pattern.

This study focuses on three variables: sea surface temperature (SST), zonal wind at 850 hPa (u850), and vertical pressure velocity (or $p$ velocity) at 500 hPa ($\omega$500) in the tropical belt between 20°S and 20°N. The vertical $p$ velocity $\omega = dp/dt$ is defined as the Lagrangian rate of change of pressure $p$ with time. Here, we plot $-\omega$500, so that positive values indicate upward large-scale motion (associated with heating in the free troposphere) and negative values indicate subsidence. The set of variables is not chosen to produce the most skillful linear inverse model, but to understand the interplay between large-scale vertical motions, zonal wind, and ocean response. Anomalies of SST, u850, and $\omega$500 are obtained by removing the mean annual cycle and linear trend obtained from the entire record.

For comparisons with the observed record, we use ERA20C, which spans the years 1900–2010. ERA20C assimilates surface pressures and surface winds over the oceans and uses sea surface temperatures from HadISST2 as lower boundary conditions (Poli et al. 2016). Because of the limited number of observations used, there are better reanalysis products available for the atmospheric state, especially for the better observed period since 1979. However, the consistency between the atmosphere and SSTs over an extended period makes the use of ERA20C attractive. We keep in mind that—especially when it comes to the vertical $p$ velocity—the reanalysis will be dominated by the model first guess rather than observations.

For data-reduction purposes all variables of each dataset were standardized with the spatially averaged standard deviation of ERA20C and projected onto the empirical orthogonal functions (EOFs) computed from ERA20C. The EOFs were computed for each variable separately and the anomalies subsequently projected onto the first 10 EOFs of $\omega$500 and u850 and the first 30 EOFs for SST. The LIMs are fitted to the state consisting of the combined principal components of $\omega$500 and u850 and SST. These variables were chosen to capture the interplay between atmospheric and oceanic key players relevant to ENSO rather than construct the most skillful LIM. The LIM is primarily used to study the impact of adding stochastic tendency perturbations to the atmospheric component, while the ocean component was unchanged. Hence, we did not include a subsurface ocean variable, which might have added forecast skill (Newman et al. 2011). While there is some sensitivity to the details of the standardization as well as the number of EOFs retained, all findings reported here hold qualitatively over a wide range of choices.

## 4. Results

### *a. Covariance evolution in model and reanalysis*

In this section we will demonstrate the LIMs' ability to capture the basic features of tropical variability. We will

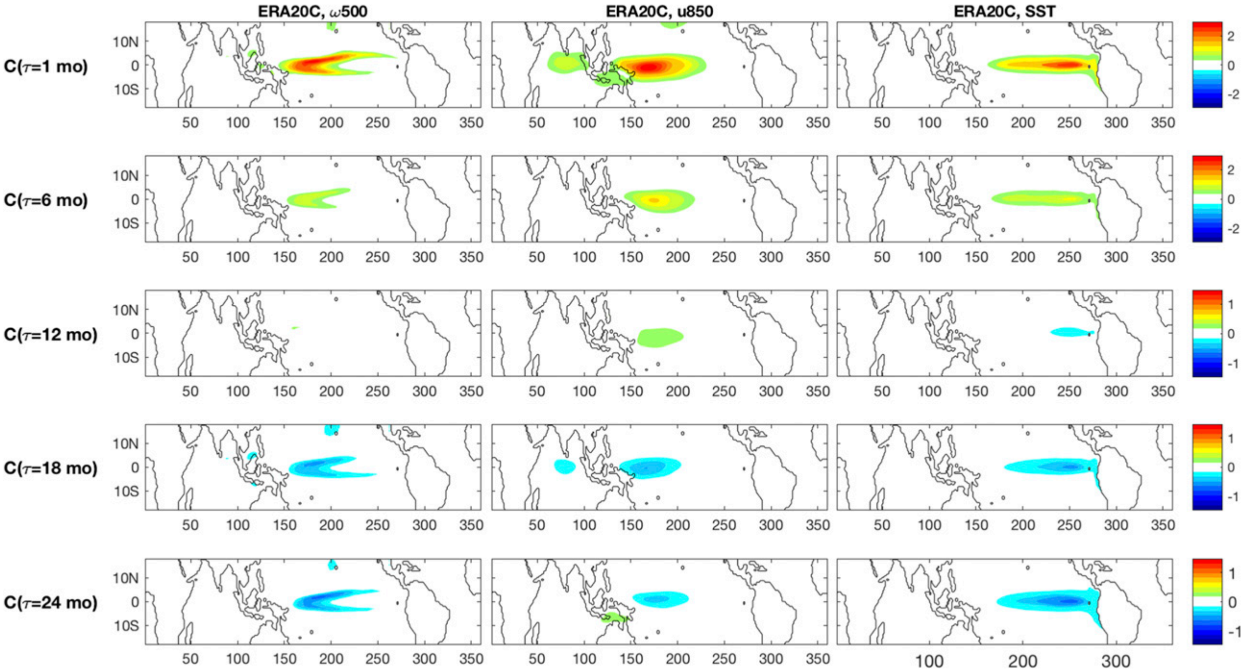

FIG. 4. Diagonal of the autocovariance matrix at lags $\tau = \{1, 6, 12, 18, 24\}$ months in ERA20C for (left) ω500, (center) u850, and (right) SST. The contour interval for lags $\tau \geq 12$ months is half that as for $\tau < 12$.

then investigate the LIMs on a mode-by-mode basis to gain insight on the mechanisms, by which SPPT affects the ENSO mode. To evaluate the model simulations and LIM, we examine the covariance evolution of ω500, u850, and SST in the tropical belt.

For ERA20C, the largest SST variance is in the tropical east and central Pacific with a pattern reminiscent of El Niño (Fig. 4). The variance swings from a positive to negative anomaly with decreasing amplitude, suggestive of a damped oscillation with a period of 4 years or so. The SST signal is accompanied by an atmospheric oscillation with the same period. For u850, the pattern of maximal variance is shifted to the western tropical Pacific with a secondary maximum over the Indian Ocean. The covariance of ω500 is boomerang shaped with the two arms extending just north and south of the equator across the Pacific basin.

For the simulations CNTL and SPPT, the centers of maximal variance are in the same east and west Pacific locations (Figs. 5, 6) indicating that the characteristic features of ENSO variability are captured by the climate model. The amplitudes in SPPT are notably smaller for all time lags, leading to a better agreement with those of ERA20C. This indicates that the oscillation in SPPT is more damped than in CNTL.

Next, linear inverse models in (5) are fitted by estimating the covariance matrix of each experiment for a time lag of $\tau_0 = 1$ month and using (6) and (7) to determine the effective feedback and noise covariance matrices. Details of the fitting procedure are described in appendix A. Note that the empirical fit yields the effective feedback and noise covariance matrices, $\mathbf{M}$ and $\tilde{\mathbf{Q}}$, which already include the effects of a potential noise-induced drift and additional noise covariance term.

The LIM captures the characteristic features of the covariance evolution in the climate simulations remarkably well (Figs. 5, 6). For brevity, the covariances are shown here only for SST and u850. The evolution of ω500 is captured similarly well and available in the supplementary material. The lagged covariance displays the same centers of variability as the climate model and captures the damped oscillation. Note, that while only 1-month lagged covariances were used, the LIM captures the pattern and amplitude of the covariance evolution over a wide range of lags up to 2 years. In particular, the LIM captures the fact that the oscillation in SPPT is more damped than that in CNTL.

As scalar metrics we compute the spatially averaged autocorrelations and autocovariances over the tropical band (Fig. 7). Consistent with the maps, the spatially averaged autocorrelation has the typical signature of a damped oscillation. We note that the autocorrelation curves for the SPPT simulation are overall in much better agreement with those in ERA20C. The LIM predicts the autocorrelation and autocovariance remarkably well up to lags of at least $\tau = 18$ months. For

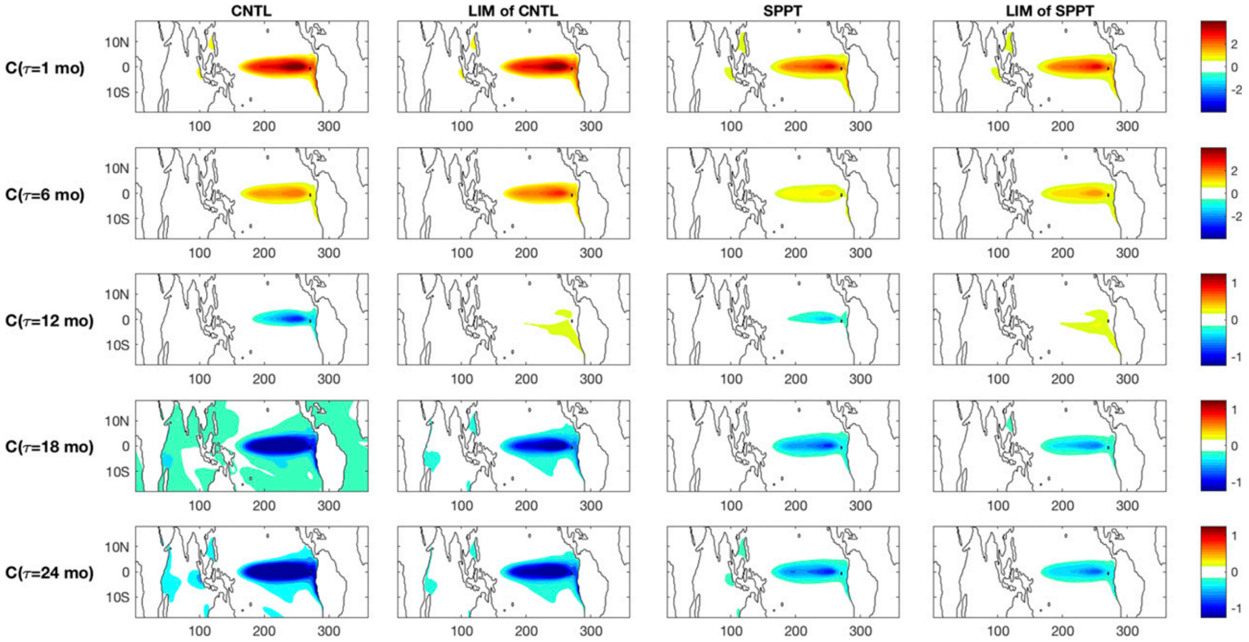

FIG. 5. Diagonal of lagged autocovariance matrix for SSTs in simulations CNTL and SPPT and lagged autocovariance matrix as predicted by a LIM fitted to CNTL and SPPT using 1-month lag covariances. Contour intervals are as in Fig. 4.

$\tau > 12$ months, the correlation curves for the GCM simulations are no longer smooth, which is an indication of insufficient sampling.

### b. Linear inverse model eigenmodes

Next, we will investigate if the differences in the LIMs can be used to understand why SPPT has a better representation of ENSO variability. Since **M** is stable, its eigenvalues are either real and negative or come in complex conjugate pairs. The associated eigenvectors or POPs correspond to the least damped modes of the linearized system (von Storch et al. 1988; Penland 1989). Since these modes decay slower than any other mode, they can be expected to play an important role in

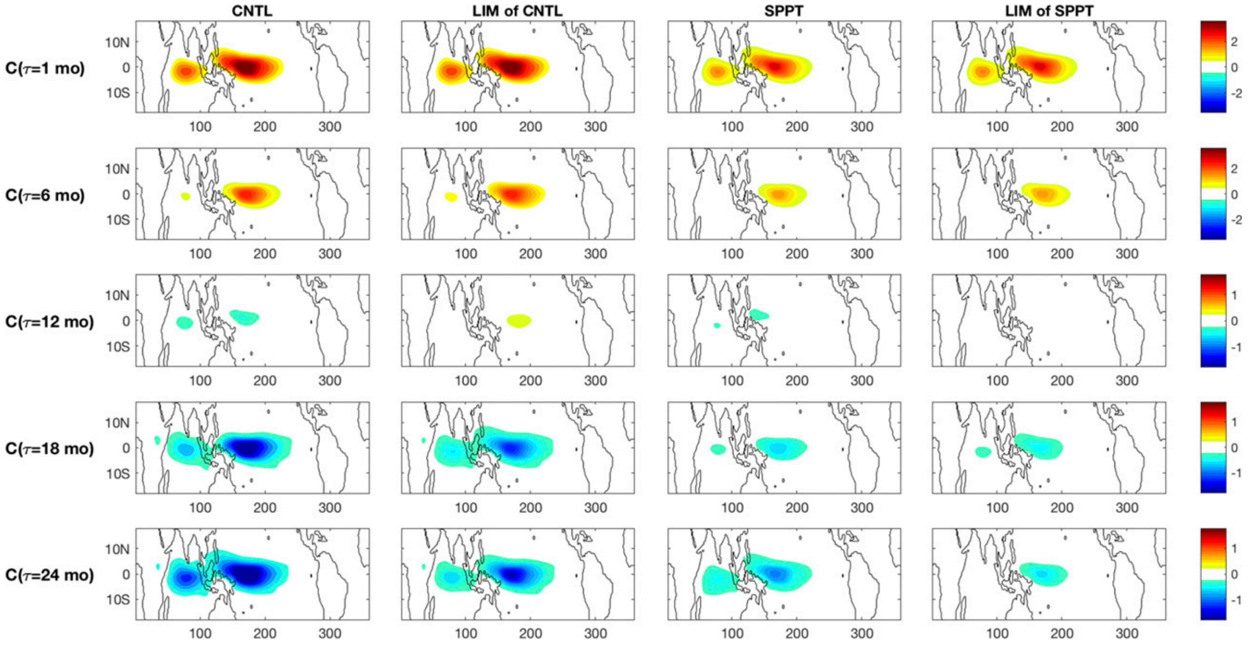

FIG. 6. As in Fig. 5, but for u850.

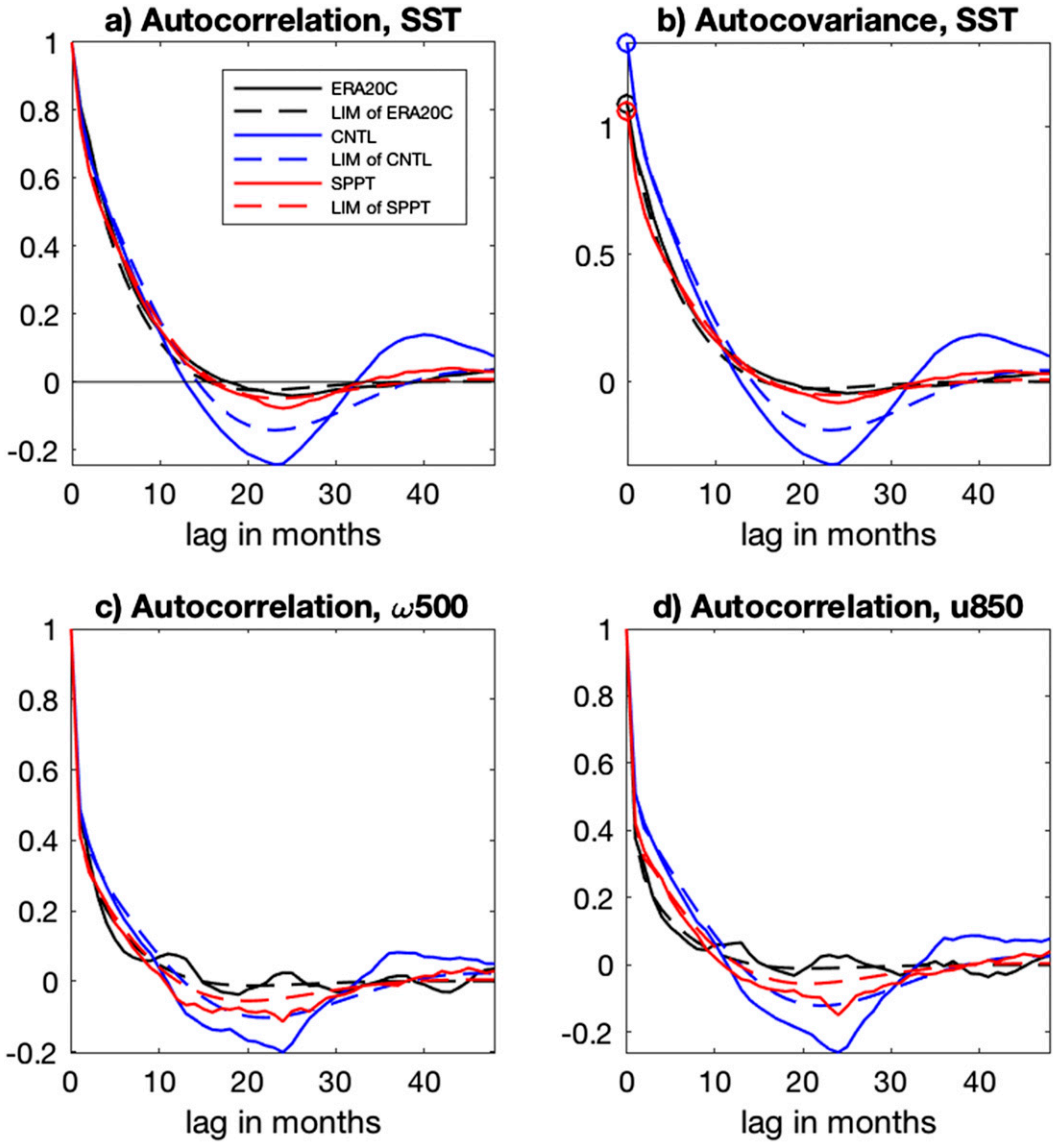

FIG. 7. (a) Autocorrelation and (b) autocovariance of SSTs averaged over the tropical band between 20°S and 20°N. Solid lines are for ERA20C (black), CNTL (blue), and SPPT (red); dashed lines are for LIM predictions. The lag-0 variance is denoted by circles. Autocorrelations for (c) $\omega$500 and (d) u850 are shown.

the system dynamics before ultimately decaying. Each oscillatory POP is complex and describes an evolving pattern that can be represented by two standing modes varying in quadrature. In other words, each POP has the form of the damped oscillator introduced in section 2. Of special interest is the least damped oscillatory POP, since its spatial pattern and variability has been associated with ENSO (Penland and Sardeshmukh 1995).

For each eigenmode of **M**, the negative inverse of the real part of the eigenvalue (i.e., its decorrelation time) is plotted in Fig. 8 against the absolute value of the imaginary part (i.e., its frequency). Modes with longer decorrelation times generally tend to be associated with lower frequencies, while modes with higher frequency tend to have less memory (Fig. 8a). For ERA20C, the least damped oscillatory mode (circled) has a period of 45 months and a damping time of 8 months. In the model experiments, this ENSO mode is associated with periods of 49 (CNTL) and 51 months (SPPT) and damping times of 17 (CNTL) and 11 (SPPT) months, respectively.

The spatial pattern of this mode is shown for each component $\omega$500, u850, and SST separately (Fig. 9).

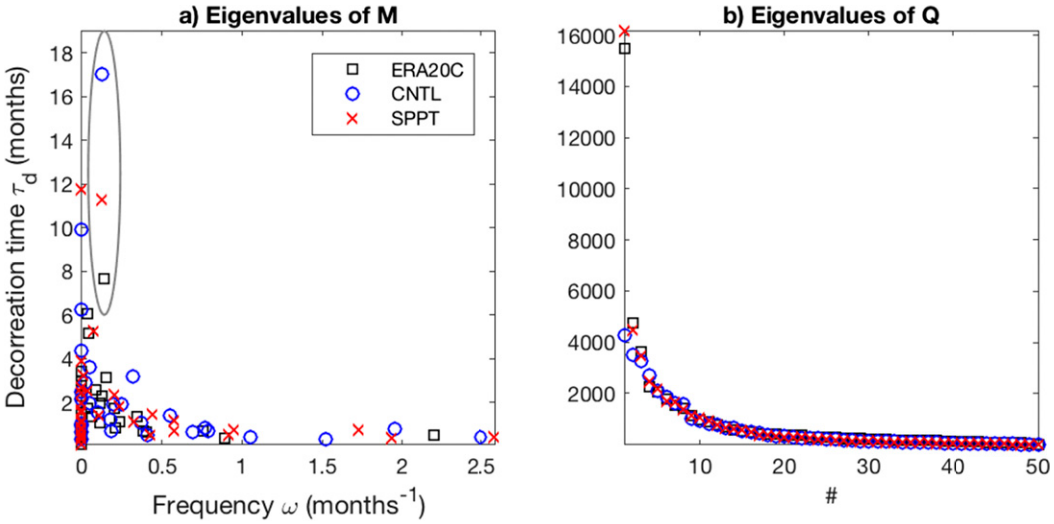

FIG. 8. Eigenvalues of the LIM (a) linear feedback matrix **M** and (b) forcing covariance matrix $\tilde{\mathbf{Q}}$. For **M**, the inverse of the real part of the eigenvalues equals the damping time scale (or decorrelation time) and is plotted against the imaginary part (equaling the frequency). Values for the least damped oscillatory mode are circled. For $\tilde{\mathbf{Q}}$, the eigenvalues are plotted as function of rank. Symbols indicate eigenvalues for ERA20C (black squares), CNTL (blue circles), and SPPT (red crosses).

Since the POPs are the empirical normal modes of the system, their sign and contour interval is arbitrary. Here, they are chosen so that the real part of the SST pattern is positively correlated with the Niño-3.4 index and the imaginary part is positively correlated with the index prior to an El Niño event. The signs for wind and vertical motion are chosen so that positive SST anomalies in the east Pacific are associated with anomalous subsidence and lower-level divergence over the Maritime Continent. The eigenvectors are normalized to have a length of unity.

The SST component of the least damped oscillatory eigenmode has the highest amplitudes in the central and east Pacific, with a pattern highly reminiscent of El Niño (Fig. 9). The u850 component has a pronounced dipole pattern with a negative center over the Maritime Continent and Indian Ocean and a positive center over the western Pacific (Figs. 9c,i,o), indicative of anomalous low-level wind divergence over the Maritime Continent. This is consistent with the anomalous subsidence over the Maritime Continent and anomalous convection over the central Pacific (Figs. 9a,g,m), as typically observed during the warm phase of ENSO.

The imaginary part of the least damped oscillatory eigenmode shows anomalous warming in the east Pacific, but as reported in other studies (Penland and Sardeshmukh 1995; Gehne et al. 2014), the anomalies are much weaker and confined to a narrow tropical band (Figs. 9f,l,v). The corresponding wind pattern shows anomalous westerlies over the Maritime Continent and western Pacific (Fig. 9d) and is highly correlated with the second EOF of u850 (not shown). The imaginary part precedes the peak pattern by a quarter of a period, which amounts to 11 months for ERA20C, 12 months for CNTL, and 13 months for SPPT. The peak pattern is then followed by the negative precursor pattern after another 12 months or so and will then develop into the La Niña peak pattern after another quarter period.

The model captures the main characteristics of the peak ENSO pattern with anomalously warm SSTs over the east Pacific corresponding to subsidence and low-level wind divergence over the Maritime Continent. While the ENSO peak and precursor *patterns* in the model simulations agree remarkably well with those from ERA20C, there are pronounced differences in the associated eigenvalues (Fig. 8a). In particular, the decorrelation time in SPPT is with $\tau_d = 11$ markedly shorter than that in CNTL ($\tau_d = 17$), but still too long compared with the $\tau_d = 8$ in ERA20C.

Given that the ENSO POP has the form of a damped oscillator, we return to the analytical results from section 2. From the perturbation experiments we know that a decrease in decorrelation time—as in experiment SPPT—is consistent with perturbations to the frequency of an oscillator. Indeed, the parameters $\nu$ and $\omega$ in Fig. 3 were chosen to produce an oscillation with a period of $T = 50$ months and decorrelation times of 17 and 11 months, reflecting the parameters of the ENSO POPs in CNTL and SPPT. The stabilization

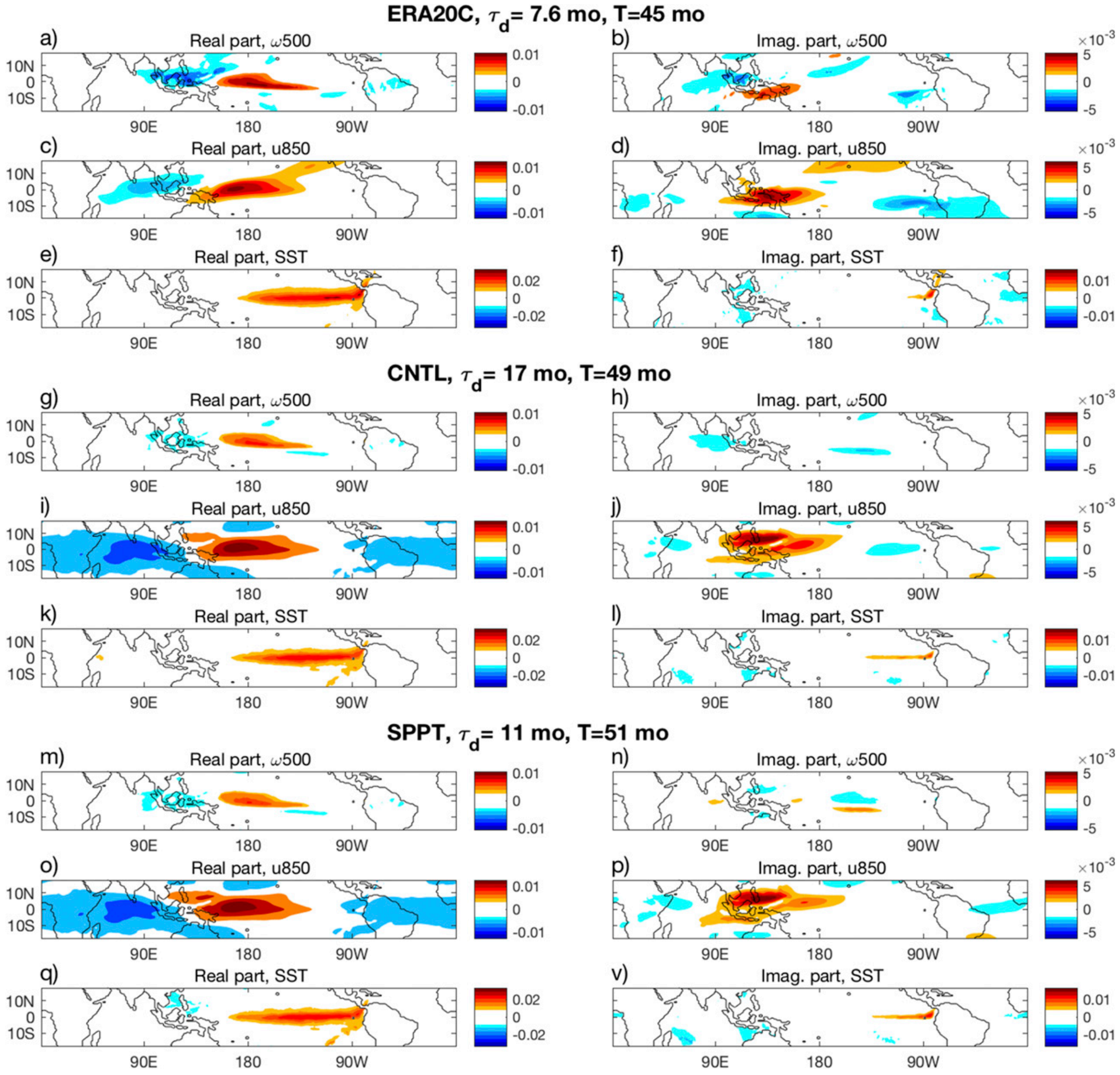

FIG. 9. (left) Real and (right) imaginary parts of the least damped oscillatory eigenmode (or principal oscillation pattern) corresponding to the mature phase of ENSO in the left panels and the characteristic precursor pattern in the right panels. Components of the mode are shown for ω500, u850, and SST for (a)–(f) ERA20C, (g)–(l) CNTL, and (m)–(r) SPPT. Decorrelation time $\tau_d$ and period $T$ are given by corresponding eigenvalues are indicated above each panel group.

from the noise-induced drift directly transfers to a broadening of the spectrum (Fig. 3d), resembling the difference in the power spectra of CNTL and SPPT (Fig. 1).

While the simple model explains the mechanisms, by which stochastic perturbations to the atmosphere can change the spectrum of ENSO, it does not provide an explanation for the observed reduction in variance (Fig. 2). Recall that perturbations to the frequency did not result in a change to the equilibrium variance in (14). We will return to this question after analyzing the second LIM component—the noise covariance matrix.

### c. *Eigenanalysis of noise covariance matrix* $\tilde{\mathbf{Q}}$

Next, we have a closer look at the noise covariance matrix $\tilde{\mathbf{Q}}$. Since $\tilde{\mathbf{Q}}$ is positive definite and real, its eigenvalues are positive and can be viewed as the variance associated with the corresponding eigenvectors. The latter form an orthogonal basis and are sometimes referred to as ''noise EOFs.'' Overall the

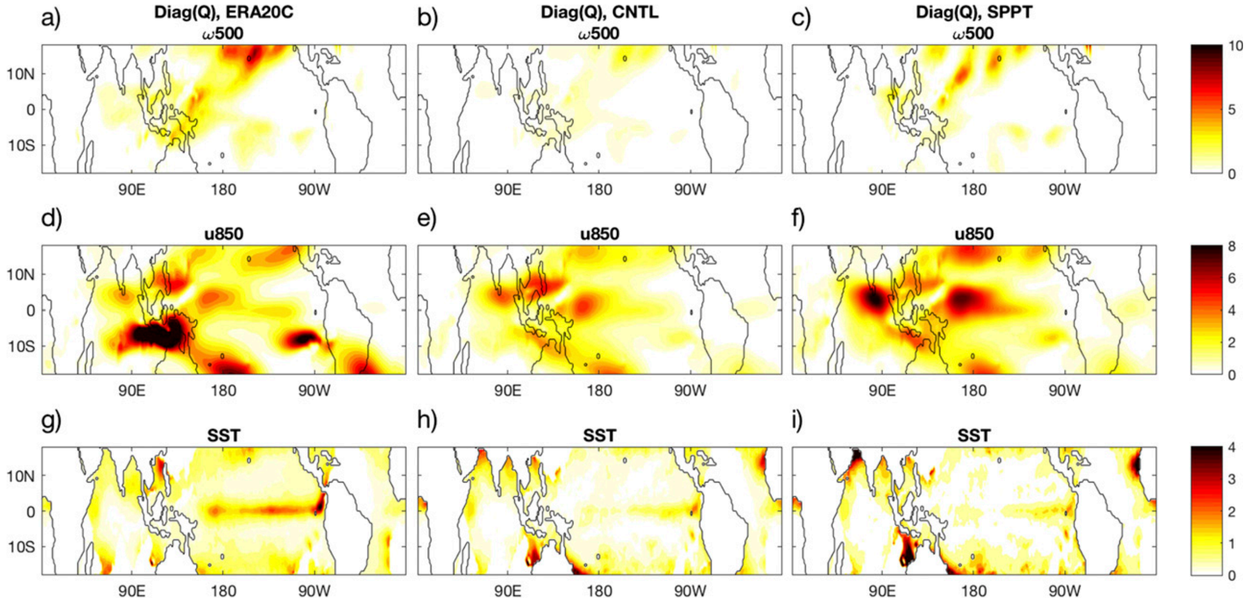

FIG. 10. Diagonal elements of the noise covariance matrix for model experiments (a),(d),(g) ERA20C; (b),(e),(h) CNTL; and (c),(f),(i) SPPT. Maps for variables (top) $\omega$500, (middle) u850, and (bottom) SST are shown.

eigenvalues decay rapidly as function of rank (Fig. 8b). For SPPT, the largest eigenvalues are markedly larger than in CNTL and are in close agreement with those in ERA20C.

Maps of the noise variance given as diagonal of $\tilde{\mathbf{Q}}$ are shown in Fig. 10. The noise variance has the largest amplitude in the zonal wind component and a very small amplitude for SST. This is consistent with the notion of atmospheric fluctuations acting as forcing for the ocean. For SPPT, the noise variance of u850 is characterized by a dipole pattern with centers over the Indian Ocean and west Pacific and an additional maximum over the Maritime Continent. These centers are also evident for ERA20C and CNTL, although for ERA20C, variability over the Maritime Continent dominates.

### d. *Impact of differences in feedback and noise covariance matrices*

Our results suggest that the stochastic perturbations of SPPT introduce a noise-induced drift resulting in a stabilization of the feedback matrix. Returning to the simple oscillator example in (5), we saw that multiplicative noise resulted in an additional, positive definite term in the effective noise covariance matrix $\tilde{\mathbf{Q}}$. For perturbations to the frequency, this additional noise term is equal and opposite to the stabilization, so that the overall variance is unchanged in (14).

Here, we attempt to separate these two effects in the climate simulations by solving for the covariance in two different versions of (7). To isolate the effect of the changes to the feedback matrix, we solve (7) for the equilibrium covariance matrix $\mathbf{C}_{\text{exp1}}$, assuming $\mathbf{M} = \mathbf{M}_{\text{SPPT}}$ and $\tilde{\mathbf{Q}} = \tilde{\mathbf{Q}}_{\text{CNTL}}$ ("exp1"):

$$\mathbf{M}_{\text{SPPT}}\mathbf{C}_{\text{exp1}} + \mathbf{C}_{\text{exp1}}\mathbf{M}_{\text{SPPT}}^{\text{T}} + \tilde{\mathbf{Q}}_{\text{CNTL}} = 0. \qquad (19)$$

This was done by transforming (19) into the eigenmode space of $\mathbf{M}_{\text{SPPT}}$, in which $\mathbf{M}_{\text{SPPT}}$ is diagonal [see appendix B, after Penland and Sardeshmukh (1995)]. The difference between the resulting equilibrium covariance matrix and that in the CNTL simulation, $\mathbf{C}_{\text{exp1}} - \mathbf{C}_{\text{CNTL}}$, is displayed in Fig. 11. For comparison, this figure shows also the difference $\mathbf{C}_{\text{SPPT}} - \mathbf{C}_{\text{CNTL}}$ obtained from solving (7) assuming $\mathbf{M} = \mathbf{M}_{\text{CNTL}}$ and $\tilde{\mathbf{Q}} = \tilde{\mathbf{Q}}_{\text{CNTL}}$ and $\mathbf{M} = \mathbf{M}_{\text{SPPT}}$ and $\tilde{\mathbf{Q}} = \tilde{\mathbf{Q}}_{\text{SPPT}}$. While the variances in Fig. 2 are computed directly from the anomaly fields, they are here derived from the LIM and transformed back from EOF space, so that the differences between Fig. 11 and Fig. 2 are the result of sampling error and EOF truncation.

Including only the changes to the feedback matrix, $\mathbf{M} = \mathbf{M}_{\text{SPPT}}$, results in an overall reduced equilibrium variance for all variables (Figs. 11b,e,h) with patterns similar to the differences between SPPT and CNTL, but weaker amplitudes. This confirms that the feedback matrix $\mathbf{M}_{\text{SPPT}}$ is more stable than $\mathbf{M}_{\text{CNTL}}$ and that the noise-induced stabilization explains about half of the reduction of variance in the SPPT simulation.

For completeness, we perform the complementary calculation of estimating the effect of only including the

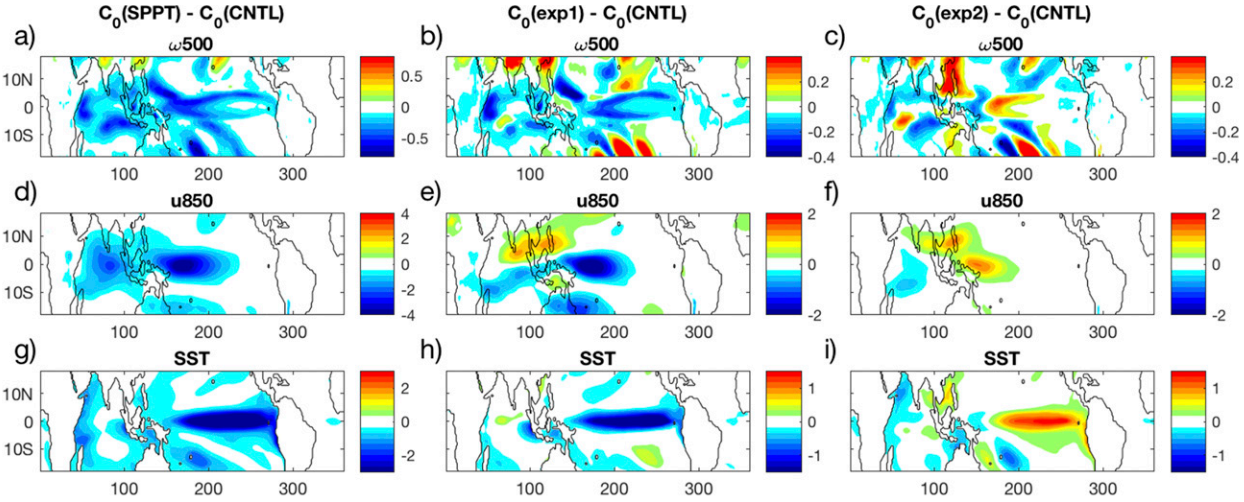

FIG. 11. (a),(d),(g) Diagonal elements of the difference between LIM covariances $\mathbf{C}_0$(CNTL) and $\mathbf{C}_0$(SPPT), obtained by solving the fluctuation–dissipation relationship for $\mathbf{M} = \mathbf{M}_{\mathrm{CNTL}}$ and $\tilde{\mathbf{Q}} = \tilde{\mathbf{Q}}_{\mathrm{CNTL}}$, and $\mathbf{M} = \mathbf{M}_{\mathrm{SPPT}}$ and $\tilde{\mathbf{Q}} = \tilde{\mathbf{Q}}_{\mathrm{SPPT}}$, respectively. (b),(e),(h) Diagonal elements of the difference between $\mathbf{C}_0$(CNTL) and the LIM covariance $\mathbf{C}_0$(exp1) assuming $\mathbf{M} = \mathbf{M}_{\mathrm{SPPT}}$ and $\tilde{\mathbf{Q}} = \tilde{\mathbf{Q}}_{\mathrm{CNTL}}$. (c),(f),(i) Difference between $\mathbf{C}_0$(CNTL) and the LIM $\mathbf{C}_0$(exp2) assuming $\mathbf{M} = \mathbf{M}_{\mathrm{CNTL}}$ and $\tilde{\mathbf{Q}} = \tilde{\mathbf{Q}}_{\mathrm{SPPT}}$. Maps for variables (top) ω500, (middle) u850, and (bottom) SST are shown.

change in the noise covariance matrix, $\tilde{\mathbf{Q}} = \tilde{\mathbf{Q}}_{\mathrm{SPPT}}$, keeping $\mathbf{M} = \mathbf{M}_{\mathrm{CNTL}}$ unchanged (“exp2”):

$$\mathbf{M}_{\mathrm{CNTL}}\mathbf{C}_{\mathrm{exp2}} + \mathbf{C}_{\mathrm{exp2}}\mathbf{M}^{\mathrm{T}}_{\mathrm{CNTL}} + \tilde{\mathbf{Q}}_{\mathrm{SPPT}} = 0. \qquad (20)$$

This results in an overall increase in the equilibrium variance when compared to CNTL (Figs. 11c,f,i). This is consistent with an additional forcing term in the noise covariance matrix and the increase in amplitude of the leading eigenvalues (Fig. 8b).

Overall, the increase of equilibrium variance in experiment exp2 is weaker than that variance decrease of exp1, which suggests that the noise-induced stabilization in $\mathbf{M}_{\mathrm{SPPT}}$ outweighs the noise-induced destabilization of $\tilde{\mathbf{Q}}_{\mathrm{SPPT}}$. While this is consistent with the overall decrease in variance in the climate simulations with SPPT, it does not explain the amplitude of the decrease nor the causes for this “asymmetry.” This manifests the limitation of the current approach, including, for example, the violation of the assumption of linearity.

## 5. Discussion: Climate simulations forced by repeating climatological annual cycle of SST

### a. *Variability of monthly anomalies*

We have hypothesized here that the perturbations introduced by SPPT to the atmospheric component of CCSM4 perturb the frequency of the El Niño–Southern Oscillation, resulting in a noise-induced drift that enhances the damping of ENSO. To further test this hypothesis, we ask what the effect of SPPT would be if there was no ENSO. The simple model suggests that if there is no oscillation, there is no frequency to perturb and presumably no stabilizing noise-induced drift. To confirm this, we performed two additional 10-yr uncoupled atmospheric GCM integrations with and without SPPT using the atmospheric component of CCSM4 with a prescribed repeating climatological annual cycle of SSTs as boundary forcing. By experimental design, there is no ENSO, indeed no interannual SST variability, in these uncoupled integrations.

Comparing the variance of zonal wind and vertical $p$ velocities in the two simulations shows that their differences are very small (Fig. 12). In most places, the differences are not statistically significant at the 95% confidence level, although there is a region in the western Pacific just north of the equator, where SPPT might *increase* the monthly variability in these variables. This confirms that SPPT does not reduce the interannual wind variability in the absence of interannual SST variability.

This is consistent with the results of Christensen et al. (2017), who also performed uncoupled atmospheric simulations, but with observed interannually varying SSTs as lower boundary forcing. These simulations have the ENSO signal in the lower boundary forcing, but no freely evolving coupled ENSO mode. This study found that introducing SPPT reduced the atmospheric variability, but the change was less pronounced than in the fully coupled simulation. In conclusion, the model must have a freely evolving coupled

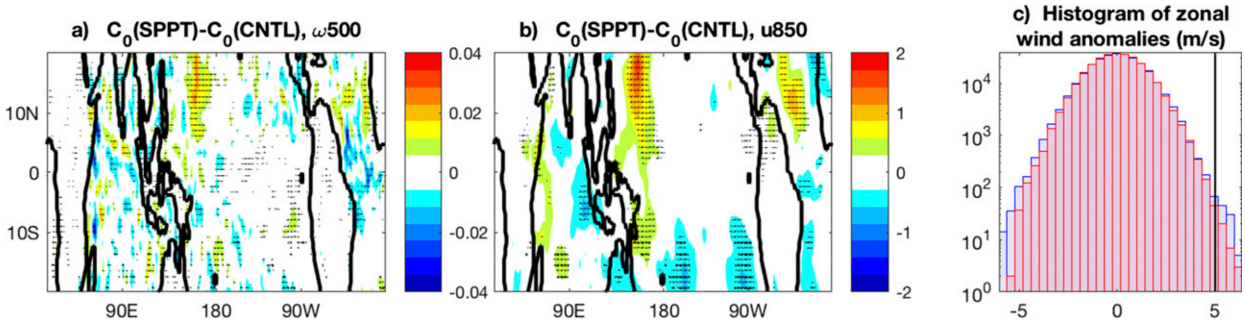

FIG. 12. Difference in variance of monthly anomalies of (a) $\omega$500 and (b) u850 in 10-yr-long simulations forced by repeating climatological SSTs. Shown is the difference between simulations with and without SPPT. Note that the contour interval in (a) is one-fourth and in (b) it is half of that in the respective panels in Figs. 2c and 2f. Differences that are statistically significant at the 95% confidence level are stippled. (c) Histogram of 5-day running mean zonal wind anomalies in CNTL (blue) and SPPT (red). Westerly wind bursts are defined as zonal wind anomalies exceeding 5 m s$^{-1}$ (black vertical line).

ENSO mode for SPPT to have a strong impact on interannual variability.

### b. *Westerly wind bursts*

Previous studies demonstrated that extreme westerly wind anomalies over the equatorial western-central Pacific—so-called westerly wind bursts (WWBs)—can play a key role in the outbreak of El Niño events, since they have the potential to trigger eastward-propagating oceanic Kelvin waves, which lead to a warming in the equatorial central and eastern Pacific (e.g., McPhaden and Taft 1988; Yu and Rienecker 1998; Lengaigne et al. 2004). The state-dependent nature of the stochastic WWB forcing is thought to be particularly important (Jin et al. 2007; Levine and Jin 2010, 2017). A change of either the magnitude of WWBs or their state dependence would constitute a physical mechanism by which SPPT can influence the development and evolution of ENSO. Following Levine and Jin (2017), Christensen et al. (2017) analyzed the state dependence of WWB and found indeed a reduction in the state dependence of WWB in the simulations with SPPT. However, in coupled simulations it is extremely difficult to disentangle the causality of WWBs and SSTs in the west Pacific, since on one hand wind anomalies are thought to be the primary forcing for ocean variability, but on the other are modulated themselves by the SSTs (Tziperman and Yu 2007).

To see if the magnitude of WWBs has been changed independently of the state dependence, we analyze the distribution of zonal wind anomalies in our simulations with climatological SSTs. We take wind anomalies as the deviation from the daily climatology (Harrison and Vecchi 1997) and subsequently compute the running 5-day mean to pick out longer lasting events. WWBs are defined as events, where the smoothed anomalous zonal winds exceeded 5 m s$^{-1}$. Histograms of the zonal wind anomalies show that SPPT reduces extreme easterly as well as westerly wind anomalies (Fig. 12c). In particular, the frequency of WWBs is reduced.

Importantly, this change in the tails of 5-day running means does not imprint on the standard deviation of monthly mean anomalies (Fig. 12b). We conclude that in addition to a reduced state dependence (Christensen et al. 2017), the reduced occurrence of strong WWB in SPPT might play a key role in reducing ENSO variability. Future work will be targeted at understanding why SPPT reduces the extreme zonal wind anomalies.

## 6. Conclusions

With the aim of understanding changes in ENSO irregularity, we fitted a linear inverse model to climate simulations with and without the stochastic parameterization scheme SPPT. In particular, we set out to understand the dynamical mechanisms by which perturbations to the atmosphere reduced tropical SST and wind variability and decreased the decorrelation time of ENSO variability.

In the experiment with stochastic perturbations, the least damped oscillatory eigenmode or principal oscillation pattern (POP) is characterized by a more damped oscillation, reducing the decorrelation time of the mode from 17 to 11 months, which according to the Wiener–Khinchin theorem explains the broadening of the spectrum (Fig. 1). This is an improvement in comparison to the 20th-century reanalysis from ECMWF, in which this mode has a decorrelation time of about 8 months.

The fact that this least damped coupled mode has a pattern and period characteristic for ENSO supports the theory of ENSO as a damped oscillation of the coupled ocean–atmosphere system forced by stochastic atmospheric noise (Penland and Sardeshmukh 1995; Kleeman and Moore 1997; Moore and Kleeman 1999; Gehne et al. 2014). Note that independent of the nature of ENSO, each POP has by definition the form of a damped oscillator (von Storch et al. 1988; Penland 1989; Kleeman 2011), so that differences among LIMs can more generally be used to diagnose model differences and differences between model and nature.

Turning to the simple model of a stochastically damped linear oscillator, we studied the effect of perturbing its frequency versus its damping rate. We found that perturbations to the damping rate result in increased variance and a more peaked spectrum, whereas perturbations to the frequency reduce the temporal memory and broaden the spectrum (Fig. 3). The GCM results consisting of a decrease in decorrelation time and broadening of the spectrum are thus consistent with perturbations to the *frequency* of the least damped eigenmode of the LIM.

The perturbations to the frequency result in further stabilizing the LIM's feedback matrix. This stabilization is due to the so-called noise-induced drift. The stabilizing influence of noise in geophysical contexts has been discussed (e.g., Sardeshmukh et al. 2001, 2003) for the example of Rossby waves in a stochastically fluctuating medium. In our ENSO context, we have shown that the noise-induced stabilization of the dynamical operator is sufficiently strong to reduce the variances of SST and winds. The noise-induced variance reduction has a pattern similar to the difference between SPPT and CNTL, but weaker magnitude.

Our results also demonstrate some of the complexities of coupled Earth-system modeling and tuning. The effect of the stochastic perturbations—used here as proxy for fast-physics processes—lie in the modulation of a slow process, here the El Niño–Southern Oscillation. The effect can therefore only be studied when fully interacting with this slow process (i.e., in a fully coupled modeling framework), and was not evident in the statistics of monthly anomalies in atmospheric simulations with repeated climatological SST forcing.

While a linear inverse model cannot replace coupled climate models, analyzing the changes to the operator of the LIM on a mode-by-mode basis allows insights into the *dynamical* mechanisms, by which stochastic perturbations to the atmospheric component with time scales of 6 h can impact tropical interannual climate variability.

Future work will focus on *physical* mechanisms by which fast-physics processes impact ENSO, starting with an in-depth analysis of the impact of SPPT on westerly wind bursts. Initial results pointed to a reduction of the occurrence and magnitude of westerly wind bursts as well as a reduced state dependence (Christensen et al. 2017), which will be investigated further.

*Acknowledgments.* We thank Dr. Maria Gehne, Prof. Natalie Burls, and an anonymous reviewer for their efforts in reviewing this manuscript. Thanks also to Dr. Grant Branstator whose insightful comments improved an earlier version of this manuscript. We acknowledge numerous delightful discussions with Dr. Cecile Penland. In particular, she was the first to mention to the first and third authors that perturbations to an oscillator can stabilize the system. Thanks also to Dr. Justin Small for sharing his results on the impact of increased horizontal resolution on tropical variability and Danielle Coleman for running the coupled climate simulations. The CESM project is supported by the National Science Foundation and the Office of Science of the U.S. Department of Energy. SPPT in CESM was developed in part under EPA Grant RD-83520501.

## APPENDIX A

### Fitting a Linear Inverse Model

To obtain an empirical estimate of the feedback matrix $\hat{\mathbf{M}}$, we estimate $\hat{\mathbf{C}}_0$ and $\hat{\mathbf{C}}(\tau_0)$ for a particular time lag $\tau_0$ and solve (6) to obtain

$$\hat{\mathbf{M}}(\tau_0) = \frac{1}{\tau_0}\log[\hat{\mathbf{C}}(\tau_0)\hat{\mathbf{C}}_0^{-1}],$$

where log is the matrix logarithm and the hat "ˆ" denotes that the operator is estimated from data. For simplicity, the hat ˆ is omitted in the main body of the paper. Subsequently, an estimate of the noise covariance is obtained by inserting $\hat{\mathbf{M}}$ and $\hat{\mathbf{C}}_0$ into (7) and solving for $\hat{\tilde{\mathbf{Q}}}$. Since $\tilde{\mathbf{Q}}$ is a covariance matrix, its eigenvalues should be real and nonnegative. However, for the estimate $\hat{\tilde{\mathbf{Q}}}$ this criterion is not always met, since $\hat{\mathbf{M}}$ and $\hat{\mathbf{C}}_0$ are subject to sampling errors. Penland and Magorian (1993) and Penland and Sardeshmukh (1995) contain detailed discussions of this issue and provide practical remedies. Following their suggestions, we set negative eigenvalues of $\hat{\tilde{\mathbf{Q}}}$ to zero. The resulting empirical model [Eqs. (1) and (5)] describing the evolution of the state is called the linear inverse model (LIM; Penland 1989; Penland and Matrosova 1994) and yields skillful predictions of the coupled atmosphere–ocean system. Predictions of the lagged covariance for any lag $\tau$ can be obtained via

$$\hat{\mathbf{C}}(\tau) = e^{\hat{\mathbf{M}}\tau}\hat{\mathbf{C}}_0,$$

where we need to keep in mind that $\hat{\mathbf{M}} = \hat{\mathbf{M}}_{\tau_0}$ and $\hat{\tilde{\mathbf{Q}}} = \hat{\tilde{\mathbf{Q}}}_{\tau_0}$ have been estimated using a particular lag $\tau_0$. Ideally, the validity of the assumptions necessary to fit a LIM need to be tested and a comprehensive list of tests is laid out in Penland and Sardeshmukh (1995). In particular, the estimates of the $\hat{\mathbf{M}}$ and $\hat{\hat{\mathbf{Q}}}$ should be relatively independent of $\tau_0$ as long as $\tau_0 > \tau_{\text{crit}}$, where $\tau_{\text{crit}}$ is the smallest time scale where the system can be approximated by a linear process (DelSole 2000; Berner 2005). Penland and Sardeshmukh (1995) refer to this as a "$\tau$ test." Here, we will not conduct any of the proposed tests, but will demonstrate the validity of the LIM merely by comparing the covariance evolution of the model to that predicted by the LIM (Figs. 5, 6).

The theory presented in this section makes the assumption that the noise is white (i.e., that it is $\delta$ correlated in time). However, the stochastic parameterization in the GCM is written as a red-noise process with a decorrelation time of 6 h. More generally, even fast physical processes tend to be continuous and hence are never $\delta$ correlated. Generally speaking, it is still possible to describe such a system stochastically, as long as the decorrelation time of the finitely correlated fast processes are much smaller than those governing the system dynamics (Horsthemke and Levefer 1984; Penland 2003). An example of the impact of generating stochastic perturbations with a red rather than white spectrum is given for the example of the Rossby wave response in Sardeshmukh et al. (2003).

## APPENDIX B

### Derivation of Covariance Matrix for a Linear Stochastic Process

In fitting a LIM, the zero-lag and lagged covariance matrices from an empirical dataset are used to estimate the feedback and noise covariance matrices. However, for certain applications, we might want to reverse this process and derive the zero-lag covariance matrix $\mathbf{C}_0$ from the feedback and noise covariance matrices. For this purpose, we prescribe $\mathbf{M}$ and $\hat{\mathbf{Q}}$ in the fluctuation–dissipation relationship in (7), and solve for the covariance matrix $\mathbf{C}_0$. To solve for $\mathbf{C}_0$, (3) is transformed into normal mode space (Penland and Sardeshmukh 1995):

$$\boldsymbol{\beta}\mathbf{D}_0 + \mathbf{D}_0\boldsymbol{\beta}^{\star} + \mathbf{A} = 0, \qquad \text{(B1)}$$

where $\mathbf{v}$ and $\mathbf{w}^{\mathrm{T}}$ are the right and adjoint eigenvectors, respectively, and $\boldsymbol{\beta} = \mathbf{w}^{\mathrm{T}}\mathbf{M}\mathbf{w}^{\star}$, $\mathbf{D}_0 = \mathbf{w}^{\mathrm{T}}\mathbf{C}_0\mathbf{w}^{\star}$, and $\mathbf{A} = \mathbf{w}^{\mathrm{T}}\mathbf{Q}\mathbf{w}^{\star}$. Since $\boldsymbol{\beta}$ is diagonal, (B1) can be rewritten in component form:

$$\boldsymbol{\beta}_i\mathbf{D}_{ij} + \mathbf{D}_{ij}\boldsymbol{\beta}_j^{\star} + \mathbf{A}_{ij} = 0$$

and solved for the covariance matrix in normal mode space:

$$\mathbf{D}_{ij} = -\mathbf{A}_{ij}/(\boldsymbol{\beta}_i + \boldsymbol{\beta}_j^{\star}).$$

Once the elements of $\mathbf{D}_0$ are obtained, the covariance matrix in physical space is derived as

$$\mathbf{C}_0 = \mathbf{v}\mathbf{D}_0\mathbf{v}^{\dagger},$$

where † denotes the complex conjugate transpose.

## REFERENCES

Alexander, M. A., L. Matrosova, C. Penland, J. D. Scott, and P. Chang, 2008: Forecasting Pacific SSTs: Linear inverse model predictions of the PDO. *J. Climate*, **21**, 385–402, https://doi.org/10.1175/2007JCLI1849.1.

Balmaseda, M. A., M. K. Davey, and D. L. Anderson, 1995: Decadal and seasonal dependence of ENSO prediction skill. *J. Climate*, **8**, 2705–2715, https://doi.org/10.1175/1520-0442(1995)008<2705:DASDOE>2.0.CO;2.

Berner, J., 2005: Linking nonlinearity and non-Gaussianity of planetary wave behavior by the Fokker–Planck equation. *J. Atmos. Sci.*, **62**, 2098–2117, https://doi.org/10.1175/JAS3468.1.

——, G. Shutts, M. Leutbecher, and T. Palmer, 2009: A spectral stochastic kinetic energy backscatter scheme and its impact on flow-dependent predictability in the ECMWF ensemble prediction system. *J. Atmos. Sci.*, **66**, 603–626, https://doi.org/10.1175/2008JAS2677.1.

——, and Coauthors, 2017: Stochastic parameterization: Toward a new view of weather and climate models. *Bull. Amer. Meteor. Soc.*, **98**, 565–588, https://doi.org/10.1175/BAMS-D-15-00268.1.

Buizza, R., M. Miller, and T. N. Palmer, 1999: Stochastic representation of model uncertainties in the ECMWF ensemble prediction system. *Quart. J. Roy. Meteor. Soc.*, **125**, 2887–2908, https://doi.org/10.1002/qj.49712556006.

Burgers, G., and D. B. Stephenson, 1999: The normality of El Niño. *Geophys. Res. Lett.*, **26**, 1027–1030, https://doi.org/10.1029/1999GL900161.

Christensen, H., J. Berner, D. R. Coleman, and T. Palmer, 2017: Stochastic parameterization and El Niño–Southern Oscillation. *J. Climate*, **30**, 17–38, https://doi.org/10.1175/JCLI-D-16-0122.1.

Danabasoglu, G., S. C. Bates, B. P. Briegleb, S. R. Jayne, M. Jochum, W. G. Large, S. Peacock, and S. G. Yeager, 2012: The CCSM4 ocean component. *J. Climate*, **25**, 1361–1389, https://doi.org/10.1175/JCLI-D-11-00091.1.

DelSole, T., 2000: A fundamental limitation of Markov models. *J. Atmos. Sci.*, **57**, 2158–2168, https://doi.org/10.1175/1520-0469(2000)057<2158:AFLOMM>2.0.CO;2.

DiNezio, P. N., and C. Deser, 2014: Nonlinear controls on the persistence of La Niña. *J. Climate*, **27**, 7335–7355, https://doi.org/10.1175/JCLI-D-14-00033.1.

Farrell, B. F., and P. J. Ioannou, 1993: Stochastic forcing of the linearized Navier–Stokes equations. *Phys. Fluids*, **5A**, 2600–2609, https://doi.org/10.1063/1.858894.

Flato, G., and Coauthors, 2013: Evaluation of climate models. *Climate Change 2013: The Physical Science Basis*, T. F. Stocker et al., Eds., Cambridge University Press, 741–866, https://doi.org/10.1017/CBO9781107415324.020.

Flügel, M., P. Chang, and C. Penland, 2004: The role of stochastic forcing in modulating ENSO predictability. *J. Climate*, **17**, 3125–3140, https://doi.org/10.1175/1520-0442(2004)017<3125:TROSFI>2.0.CO;2.

Gardiner, C. W., 1983: *Handbook of Stochastic Methods for Physics, Chemistry and the Natural Sciences*. Springer Verlag, 442 pp.

Gehne, M., R. Kleeman, and K. E. Trenberth, 2014: Irregularity and decadal variation in ENSO: A simplified model based on principal oscillation patterns. *Climate Dyn.*, **43**, 3327–3350, https://doi.org/10.1007/s00382-014-2108-6.

Gent, P. R., and Coauthors, 2011: The Community Climate System Model version 4. *J. Climate*, **24**, 4973–4991, https://doi.org/10.1175/2011JCLI4083.1.

Guilyardi, E., A. Wittenberg, A. Fedorov, M. Collins, C. Wang, A. Capotondi, G. J. Van Oldenborgh, and T. Stockdale, 2009: Understanding El Niño in ocean–atmosphere general circulation models: Progress and challenges. *Bull. Amer. Meteor. Soc.*, **90**, 325–340, https://doi.org/10.1175/2008BAMS2387.1.

Harrison D. E., and G. A. Vecchi, 1997: Westerly wind events in the tropical Pacific, 1986–95. *J. Climate*, **10**, 3131–3156, https://doi.org/10.1175/1520-0442(1997)010<3131:WWEITT>2.0.CO;2.

Horsthemke, W., and R. Levefer, 1984: *Noise-Induced Transitions*. Springer Verlag, 318 pp.

Hunke, E. C., and W. H. Lipscomb, 2008: CICE: The Los Alamos Sea Ice Model user's manual, version 4. Los Alamos National Laboratory Tech. Rep. LA-CC-06-012, 76 pp.

Jin, F.-F., L. Lin, A. Timmermann, and J. Zhao, 2007: Ensemble-mean dynamics of the ENSO recharge oscillator under state-dependent stochastic forcing. *Geophys. Res. Lett.*, **34**, L03807, https://doi.org/10.1029/2006GL027372.

Kleeman, R., 2011: Spectral analysis of multidimensional stochastic geophysical models with an application to decadal ENSO variability. *J. Atmos. Sci.*, **68**, 13–25, https://doi.org/10.1175/2010JAS3546.1.

——, and A. M. Moore, 1997: A theory for the limitation of ENSO predictability due to stochastic atmospheric transients. *J. Atmos. Sci.*, **54**, 753–767, https://doi.org/10.1175/1520-0469(1997)054<0753:ATFTLO>2.0.CO;2.

Latif, M., T. Barnett, M. Cane, M. Flügel, N. E. Graham, H. von Storch, J.-S. Xu, and S. Zebiak, 1994: A review of ENSO prediction studies. *Climate Dyn.*, **9**, 167–179, https://doi.org/10.1007/BF00208250.

Lawrence, D. M., and Coauthors, 2011: Parameterization improvements and functional and structural advances in version 4 of the Community Land Model. *J. Adv. Model. Earth Syst.*, **3**, M03001, https://doi.org/10.1029/2011MS00045.

Lengaigne, M., E. Guilyardi, J.-P. Boulanger, C. Menkes, P. Delecluse, P. Inness, J. Cole, and J. Slingo, 2004: Triggering of El Niño by westerly wind events in a coupled general circulation model. *Climate Dyn.*, **23**, 601–620, https://doi.org/10.1007/s00382-004-0457-2.

Leutbecher, M., and Coauthors, 2017: Stochastic representations of model uncertainties at ECMWF: State of the art and future vision. *Quart. J. Roy. Meteor. Soc.*, **143**, 2315–2339, https://doi.org/10.1002/qj.3094.

Levine, A. F., and F.-F. Jin, 2010: Noise-induced instability in the ENSO recharge oscillator. *J. Atmos. Sci.*, **67**, 529–542, https://doi.org/10.1175/2009JAS3213.1.

——, and ——, 2017: A simple approach to quantifying the noise–ENSO interaction. Part I: Deducing the state-dependency of the windstress forcing using monthly mean data. *Climate Dyn.*, **48**, 1–18, https://doi.org/10.1007/s00382-015-2748-1.

McPhaden, M. J., and B. A. Taft, 1988: Dynamics of seasonal and intraseasonal variability in the eastern equatorial Pacific. *J. Phys. Oceanogr.*, **18**, 1713–1732, https://doi.org/10.1175/1520-0485(1988)018<1713:DOSAIV>2.0.CO;2.

Moore, A. M., and R. Kleeman, 1999: Stochastic forcing of ENSO by the intraseasonal oscillation. *J. Climate*, **12**, 1199–1220, https://doi.org/10.1175/1520-0442(1999)012<1199:SFOEBT>2.0.CO;2.

Newman, M., and P. D. Sardeshmukh, 2017: Are we near the predictability limit of tropical Indo-Pacific sea surface temperatures? *Geophys. Res. Lett.*, **44**, 8520–8529, https://doi.org/10.1002/2017GL074088.

——, ——, and C. Penland, 2009: How important is air–sea coupling in ENSO and MJO evolution? *J. Climate*, **22**, 2958–2977, https://doi.org/10.1175/2008JCLI2659.1.

——, M. A. Alexander, and J. D. Scott, 2011: An empirical model of tropical ocean dynamics. *Climate Dyn.*, **37**, 1823, https://doi.org/10.1007/s00382-011-1034-0.

Palmer, T. N., 2001: A nonlinear dynamical perspective on model error: A proposal for non-local stochastic-dynamic parameterization in weather and climate prediction models. *Quart. J. Roy. Meteor. Soc.*, **127**, 279–304, https://doi.org/10.1002/qj.49712757202.

——, R. Buizza, F. Doblas-Reyes, T. Jung, M. Leutbecher, G. Shutts, M. Steinheimer, and A. Weisheimer, 2009: Stochastic parametrization and model uncertainty. ECMWF Tech. Memo. 598, 44 pp., https://www.ecmwf.int/sites/default/files/elibrary/2009/11577-stochastic-parametrization-and-model-uncertainty.pdf.

Penland, C., 1989: Random forcing and forecasting using principal oscillation pattern analysis. *Mon. Wea. Rev.*, **117**, 2165–2185, https://doi.org/10.1175/1520-0493(1989)117<2165:RFAFUP>2.0.CO;2.

——, 2003: Noise out of chaos and why it won't go away. *Bull. Amer. Meteor. Soc.*, **84**, 921–926, https://doi.org/10.1175/BAMS-84-7-Penland.

——, and T. Magorian, 1993: Prediction of Niño 3 sea surface temperatures using linear inverse modeling. *J. Climate*, **6**, 1067–1076, https://doi.org/10.1175/1520-0442(1993)006<1067:PONSST>2.0.CO;2.

——, and L. Matrosova, 1994: A balance condition for stochastic numerical models with application to the El Niño–Southern Oscillation. *J. Climate*, **7**, 1352–1372, https://doi.org/10.1175/1520-0442(1994)007<1352:ABCFSN>2.0.CO;2.

——, and P. Sardeshmukh, 1995: The optimal growth of tropical sea surface temperature anomalies. *J. Climate*, **8**, 1999–2024, https://doi.org/10.1175/1520-0442(1995)008<1999:TOGOTS>2.0.CO;2.

Poli, P., and Coauthors, 2016: ERA-20C: An atmospheric reanalysis of the twentieth century. *J. Climate*, **29**, 4083–4097, https://doi.org/10.1175/JCLI-D-15-0556.1.

Sardeshmukh, P., and P. Sura, 2009: Reconciling non-Gaussian climate statistics with linear dynamics. *J. Climate*, **22**, 1193–1207, https://doi.org/10.1175/2008JCLI2358.1.

——, C. Penland, and M. Newman, 2001: Rossby waves in a stochastically fluctuating medium. *Stochastic Climate Models*, P. Imkeller and J.-S. von Storch, Eds., Progress in Probability Series, Vol. 49, Birkäuser Verlag, 369–384, https://doi.org/10.1007/978-3-0348-8287-3_17.

——, ——, and ——, 2003: Drifts induced by multiplicative red noise with application to climate. *EPL*, **63**, 498, https://doi.org/10.1209/epl/i2003-00550-y.

Shin, S.-I., P. D. Sardeshmukh, and K. Pegion, 2010: Realism of local and remote feedbacks on tropical sea surface temperatures in climate models. *J. Geophys. Res.*, **115**, D21110, https://doi.org/10.1029/2010JD013927.

Small, R. J., R. A. Tomas, and F. O. Bryan, 2014: Storm track response to ocean fronts in a global high-resolution climate model. *Climate Dyn.*, **43**, 805–828, https://doi.org/10.1007/s00382-013-1980-9.

Tziperman, E., and L. Yu, 2007: Quantifying the dependence of westerly wind bursts on the large-scale tropical Pacific SST. *J. Climate*, **20**, 2760–2768, https://doi.org/10.1175/JCLI4138a.1.

von Storch, H., T. Bruns, I. Fischer-Bruns, and K. Hasselmann, 1988: Principal oscillation pattern analysis of the 30- to 60-day oscillation in general circulation model equatorial troposphere. *J. Geophys. Res.*, **93**, 11 022–11 036, https://doi.org/10.1029/JD093iD09p11022.

——, G. Bürger, R. Schnur, and J.-S. von Storch, 1995: Principal oscillation patterns: A review. *J. Climate*, **8**, 377–400, https://doi.org/10.1175/1520-0442(1995)008<0377:POPAR>2.0.CO;2.

Weisheimer, A., S. Corti, T. Palmer, and F. Vitart, 2014: Addressing model error through atmospheric stochastic physical parametrizations: Impact on the coupled ECMWF seasonal forecasting system. *Philos. Trans. Roy. Soc. London*, **372A**, 2018, https://doi.org/10.1098/rsta.2013.0290.

Wu, D.-H., D. L. Anderson, and M. K. Davey, 1994: ENSO prediction experiments using a simple ocean-atmosphere model. *Tellus*, **46A**, 465–480, https://doi.org/10.3402/tellusa.v46i4.15493.

Xu, J.-S., and H. von Storch, 1990: Predicting the state of the Southern Oscillation using principal oscillation pattern analysis. *J. Climate*, **3**, 1316–1329, https://doi.org/10.1175/1520-0442(1990)003<1316:PTSOTS>2.0.CO;2.

Yeh, S.-W., and B. P. Kirtman, 2006: Origin of decadal El Niño–Southern Oscillation–like variability in a coupled general circulation model. *J. Geophys. Res.*, **111**, C01009, https://doi.org/10.1029/2005JC002985.

Yu, L., and M. M. Rienecker, 1998: Evidence of an extratropical atmospheric influence during the onset of the 1997–98 El Niño. *Geophys. Res. Lett.*, **25**, 3537–3540, https://doi.org/10.1029/98GL02628.

Zanna, L., 2012: Forecast skill and predictability of observed Atlantic sea surface temperatures. *J. Climate*, **25**, 5047–5056, https://doi.org/10.1175/JCLI-D-11-00539.1.